

Integral force acting on a body due to local flow structures

J.-Z. WU^{1,2†}, X.-Y. LU³ AND L.-X. ZHUANG³

¹State Key Laboratory for Turbulence and Complex System, Peking University, Beijing, China

²University of Tennessee Space Institute, Tullahoma, TN 37388, USA

³University of Science and Technology of China, Hefei, Anhui 230026, China

(Received 27 January 2006 and in revised form 23 October 2006)

The forces exerted on a body moving through a fluid depend strongly on the local dynamic processes and structures generated by the body motion, such as flow separation, vortices, etc. A detailed and quantitative understanding of the effects of these processes and structures on the instantaneous overall force characteristics is of fundamental significance, and may improve our capabilities for flow analysis and control. In the present study, some unconventional force expressions based on ‘derivative-moment transformations’, which can have a rich variety of forms for the same flow field, are used to provide better insight into local dynamics. In particular, we apply jointly three alternative unconventional force expressions to analyse two numerical solutions of unsteady and viscous circular-cylinder flows. The results confirm the exactness of the expressions and, more importantly, provide a unified understanding of the specific influence on the force of each individual flow structure at its different evolution stages.

1. Introduction

Whenever an integrated quantity directly derived from the fundamental fluid dynamic equations is to be analysed, for example the total force and moment in external flow problems, a simple but very useful way to obtain insight into the relevant physics is to perform an integration by parts via the Gauss and Stokes theorems. Then the original integrand is transformed to the moments of its spatial derivatives which, if necessary, can be replaced by other terms in the differential motion equations to explicitly reveal the effect of various local dynamic processes and structures on the integrated performance.

This kind of transformation can be traced back to Thomson (1883), who expressed the total momentum (the integral of $\rho \mathbf{u}$) of an incompressible flow in a domain \mathcal{D} as the moment of the hydrodynamic impulse (the integral of $\rho \mathbf{x} \times \boldsymbol{\omega}$, where $\boldsymbol{\omega} = \nabla \times \mathbf{u}$ is the vorticity) plus a boundary integral over $\partial \mathcal{D}$. Then, as cited in Truesdell (1954), Föppl in 1897 expressed the total vorticity in \mathcal{D} as the integral of the moment of the normal vorticity on $\partial \mathcal{D}$, and thereby stated the famous total vorticity conservation theorem. These transformations and similar ones, including higher-order moments, have appeared extensively in fluid dynamics textbooks, e.g. Lamb (1932), Truesdell (1954), Batchelor (1967), Lighthill (1986), and Saffman (1992), among others, indicating their wide applicability beyond the force and moment

† Author to whom correspondence should be addressed: jzwu@mech.pku.edu.cn, jzwu@utsi.edu

expressions. It seems that all these transformations deserve a common name; here we call them the derivative-moment transformations (DMT), a list of which is presented by Wu, Ma & Zhou (2006, henceforth referred to as WMZ).

Progress in applying DMT to external aerodynamics was made by Wu (1981; see also Wu 2005), who formulated a systematic and general vorticity moment theory for the total force and moment experienced by a body moving through an incompressible fluid at rest at infinity, in terms of the rate of change of the first and second integrated moments of the vorticity. The classic circulation theory, including the two-dimensional Kutta–Joukowski formula for the lift and Prandtl's three-dimensional lifting-line theory, can be interpreted as special cases of Wu's theory under particular assumptions.

Wu's theory has motivated a series of investigations into unconventional force–moment expressions using various similar transformations over the last two decades. Wu & Wu (1993, 1996) developed a general viscous compressible force–moment theory in terms of the boundary vorticity flux, which has been applied to various external and internal aerodynamic diagnosis and design problems from low- to high-Mach-number flows (e.g. Wu *et al.* 1999; Zhu 2000; Li & Guo 2005; Guo *et al.* 2006).

On the other hand, with the aim of using the experimentally measured velocity field to calculate the total force in complex unsteady incompressible separated flows, Noca, Shiels & Jeon (1999) have derived and examined a few alternative expressions for the total force, such as the extension of Wu's (1981) theory to arbitrary finite domain and, more remarkably, an expression for the unsteady force solely in terms of a control-surface integral of the velocity and its derivatives. Since at present the particle image velocimetry technique cannot yield accurate flow data adjacent to a body surface, this latter expression has attracted wide attention (e.g. Jeon & Gharib 2001; Ploumhans *et al.* 2002; Graziani & Bassanini 2002; Zhu, Bearman & Graham 2002; Birch & Dickinson 2003; Tan, Thompson & Hourigan 2005). Meanwhile, Wu, Pan & Luo (2005) independently derived a pair of alternative force formulas equivalent to the control-surface expression of Noca *et al.* (1999) but in a simpler form, and demonstrated their general applicability and insensitivity to measurement uncertainty by a numerical experiment on a two-dimensional flow over a deformable body.

As demonstrated by the above progress following Wu (1981), one of the attractive features of DMT-based force and moment expressions is the rich multiple forms and wide choice of applications, although they all yield the same integrated force and moment for the same physical flow field. A specific form comes from selecting a conventional integral force formula and a special DMT identity to transform it. Consequently, some of the expressions are suitable for handling experimental data, e.g. Noca *et al.* (1999); some are convenient for analysing numerically obtained flow fields, e.g. the boundary vorticity-flux theory; and some are helpful for developing new approximate theories, e.g. Wu (1981, 2005). Even the simplest one-dimensional DMT familiar in elementary calculus has been applied by Li & Guo (2005) and Guo *et al.* (2006) to identify the key vortical flow structures dominating the total-pressure ratio and efficiency of turbojet compressors, leading to redesigned the rotor blades to significantly enlarge the stall margin.

For the same purpose of deeper physical understanding of the role of local flow structures on the force and moment at a fundamental level, there are several alternative forms, each able to capture certain typical process and structures (WMZ). Thus, for a given flow field, the same total force may come from different characteristic structures depending on a specific form, reflecting the inherent linkage among various structures. Therefore, one can apply different expressions simultaneously for the same flow, and

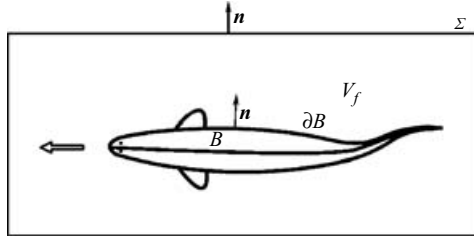


FIGURE 1. Flow domain to be analysed and notation.

thereby gain a multiple-view physical picture providing more insight than each of them on its own.

The goal of the present study is to fully explore the implications of this kind of combined use of different DMT-based expressions for complex flows. We focus on the basic physical understanding, which permits us to select a typical simple geometry (a circular cylinder) as long as the flow over it is sufficiently complicated. For clarity, we confine considerations to the total force analysis.

This paper is organized as follows. Three force expressions used in this study are presented in §2, followed by their application to two incompressible flows: an impulsively started unsteady two-dimensional flow and a three-dimensional oscillatory flow over a circular cylinder. In the latter case, both the external control surface and cylinder surface are open in the finite computational domain so that a special theoretical treatment is necessary. The mathematical formulations, numerical methods, and computed forces for both cases are given in §§3 and 4. We then make a detailed examination in §5 on how, quantitatively, the instantaneous local dynamic processes and flow structures captured by the three alternative expressions influence the force, paying special attention to the mutual relations between different expressions. Concluding remarks are given in §6.

2. Three forms of DMT-based force expressions

Let V_f be an incompressible fluid domain of spatial dimension $n = 2, 3$, surrounding a solid body B and bounded externally by an arbitrary control surface Σ , see figure 1. The body surface ∂B can be deformable and described by function $\mathbf{x}(\boldsymbol{\xi}, t)$ with Lagrangian variable $\boldsymbol{\xi}$, say $\boldsymbol{\xi} = \mathbf{x}$ at $t = 0$, such that $\mathbf{u} = \partial \mathbf{x}(\boldsymbol{\xi}, t) / \partial t \equiv \mathbf{b}(\mathbf{x}, t)$, $\mathbf{x} \in \partial B$. The control surface Σ may also deform and move with velocity $\mathbf{v}(\mathbf{x}, t)$. In this study we apply three alternative DMT-based force expressions (WMZ), keeping all the derivative terms inside the integral. The first two are

$$\mathbf{F} = -\frac{\mu}{k} \int_{V_f} \mathbf{x} \times \nabla^2 \boldsymbol{\omega} \, dV + \mathbf{F}_B + \mathbf{F}_\Sigma, \tag{2.1}$$

$$\mathbf{F} = -\rho \int_{V_f} \left(\frac{1}{k} \mathbf{x} \times \frac{\partial \boldsymbol{\omega}}{\partial t} + \mathbf{l} \right) dV - \frac{\rho}{k} \int_{\partial V_f} \mathbf{x} \times (\mathbf{n} \times \mathbf{l}) \, dS + \mathbf{F}_B + \mathbf{F}_\Sigma, \tag{2.2}$$

where $k = n - 1 = 1, 2$, $\mathbf{l} = \boldsymbol{\omega} \times \mathbf{u}$ is the Lamb vector, and ρ and $\mu = \rho \nu$ are the fluid density and viscosity, respectively. One of the boundary integrals,

$$\mathbf{F}_B = \frac{\rho}{k} \int_{\partial B} \mathbf{x} \times (\mathbf{n} \times \mathbf{a}_B) \, dS = \frac{\rho}{k} \int_{\partial B} \mathbf{x} \times \boldsymbol{\sigma}_a \, dS, \tag{2.3}$$

represents the explicit contribution of body acceleration and deformation, with $\mathbf{a}_B(\mathbf{x}, t) = \partial^2 \mathbf{x}(\boldsymbol{\xi}, t) / \partial t^2$ for $\mathbf{x} \in \partial B$. The second equality of (2.3) expresses this

contribution in terms of a constituent of the boundary vorticity flux; here we recall that (e.g. WMZ) the definition and full expression for the boundary vorticity flux on a solid surface in three-dimensional space are

$$\boldsymbol{\sigma} \equiv \mu \frac{\partial \boldsymbol{\omega}}{\partial n} = \boldsymbol{\sigma}_a + \boldsymbol{\sigma}_p + \boldsymbol{\sigma}_{\text{vis}},$$

where $\boldsymbol{\sigma}_a = \mathbf{n} \times \mathbf{a}_B$, $\boldsymbol{\sigma}_p = \mathbf{n} \times \nabla p / \rho$, and $\boldsymbol{\sigma}_{\text{vis}} = \nu(\mathbf{n} \times \nabla) \times \boldsymbol{\omega}$ are the boundary vorticity-flux constituents caused by \mathbf{a}_B , the tangential pressure gradient, and a viscous vortical effect, respectively. The other boundary integral in (2.2),

$$\mathbf{F}_\Sigma = -\frac{\mu}{k} \int_\Sigma \mathbf{x} \times [\mathbf{n} \times (\nabla \times \boldsymbol{\omega})] dS + \int_\Sigma \mu \boldsymbol{\omega} \times \mathbf{n} dS, \quad (2.4)$$

is the contribution to the force of the flow structures on the finite control surface Σ , which is a pure viscous effect.

Equation (2.1) is an extension of a result of Wu & Wu (1993) for an externally unbounded domain where the integrand is the moment of the viscous vorticity diffusion. In (2.2), the integrand is in terms of flow quantities describing the advection, such as the Lamb vector (the integral of which is known as the vortex force, e.g. Saffman 1992) and its moments. Therefore, we shall call (2.1) and (2.2) the *diffusion form* and *advection form* of the DMT-based force expressions, respectively. Evidently, (2.1) and (2.2) can be derived from each other by using the vorticity transport equation to express the viscous term by inviscid ones or vice versa, along with integration by parts. When Σ retreats to infinity where the fluid is at rest, both (2.1) and (2.2) recover Wu's (1981) vorticity moment theory.

The third force expression to be used below is an extremal case of (2.1) and (2.2) as Σ shrinks to coincide with the body surface. Then both expressions degenerate to a boundary integral over ∂B in terms of the moment of stress-related boundary vorticity fluxes. For $n = 3$ this expression is

$$\mathbf{F} = - \int_{\partial B} \rho \mathbf{x} \times \left(\frac{1}{2} \boldsymbol{\sigma}_p + \boldsymbol{\sigma}_{\text{vis}} \right) dS. \quad (2.5)$$

Note that unlike (2.3), $\boldsymbol{\sigma}_a$ does not appear explicitly in (2.5); but its effect on the force has been fully represented by its influence on $\boldsymbol{\sigma}_p$ and $\boldsymbol{\sigma}_{\text{vis}}$. For $n = 2$ and $\mathbf{a}_B = \mathbf{0}$, one simply has $\boldsymbol{\sigma} = \nu \partial \boldsymbol{\omega} / \partial n = \boldsymbol{\sigma}_p$, and instead of (2.5) the force is expressed by the moments of both the normal and tangential components of the viscous vorticity gradient $\nu \nabla \boldsymbol{\omega}$, i.e.

$$\mathbf{F} = \mu \oint_{\partial B} \left(-\mathbf{x} \times \mathbf{e}_z \frac{\partial \boldsymbol{\omega}}{\partial n} + \mathbf{x} \frac{\partial \boldsymbol{\omega}}{\partial s} \right) ds, \quad (2.6)$$

where s is the arclength increasing along the body contour in the clockwise direction and \mathbf{e}_z the unit vector in the z -direction. Equation (2.5) or (2.6) expresses the force from the characteristic quantity in the vorticity creation process. Thus we shall call them the *creation form* of the DMT-based force expression.

As stated before, the purpose of these expressions is a deeper physical understanding of the net contribution of local dynamic processes and flow structures to the force; hence, the integrand functions in the expressions need not be easily measured by experiments.

In contrast to these unconventional expressions, a familiar force formula directly derived from the momentum balance is

$$\mathbf{F} = - \int_{\partial B} (-p \mathbf{n} + \mu \boldsymbol{\omega} \times \mathbf{n}) dS, \quad (2.7)$$

where the pressure is a global quantity to which the net contributions of local dynamic processes and flow structures are unclear. However, we will use (2.7) to check the validity of the three DMT forms.

3. Two-dimensional impulsively started flow over a circular cylinder

3.1. Force formulas adopted

Our first numerical example is the two-dimensional impulsively started unsteady separated flow over a stationary circular cylinder with unit radius. We set the origin of x at the centre of the cylinder and choose the outer variable boundary Σ of the analysis domain as concentric circles of radii $r \geq 1$. In polar coordinates (r, θ) with the x -axis in the direction of $\theta = 0$, by (2.1) and (2.4) where the two viscous terms can be cast as the normal and tangential components of $\mu \nabla \omega$, the drag and lift of the cylinder in the diffusion form each have one field integral and two boundary integrals: $D(t) = D_{F1} + D_{B1} + D_{B2}$ and $L(t) = L_{F1} + L_{B1} + L_{B2}$, where

$$D_{F1} = -\mu \int_{V_f} y \nabla^2 \omega \, dS, \tag{3.1a}$$

$$D_{B1} = \mu r^2 \oint_{\Sigma} \frac{\partial \omega}{\partial r} \sin \theta \, d\theta, \quad D_{B2} = -\mu \oint_{\Sigma} \frac{1}{r} \frac{\partial \omega}{\partial \theta} \cos \theta \, d\theta, \tag{3.1b}$$

$$L_{F1} = \mu \int_{V_f} x \nabla^2 \omega \, dV, \tag{3.1c}$$

$$L_{B1} = -\mu r^2 \oint_{\Sigma} \frac{\partial \omega}{\partial r} \cos \theta \, d\theta, \quad L_{B2} = \mu \oint_{\Sigma} \frac{1}{r} \frac{\partial \omega}{\partial \theta} \sin \theta \, d\theta. \tag{3.1d}$$

Note that in this cylinder-flow example the integrands of field integrals are expressed in Cartesian coordinates, while those in boundary integrals are in polar coordinates. Then, in advection form (2.2), each of D_{F1} and L_{F1} can be further split into two field integrals and one boundary integral: $D_{F1} = D_{F2} + D_{F3} + D_{B3}$ and $L_{F1} = L_{F2} + L_{F3} + L_{B3}$, where

$$D_{F2} = -\rho \int_{V_f} y \frac{\partial \omega}{\partial t} \, dS, \quad D_{F3} = \rho \int_{V_f} v \omega \, dS, \tag{3.2a}$$

$$D_{B3} = \rho R \oint_{\Sigma} \omega u_r \sin \theta \, d\theta, \tag{3.2b}$$

$$L_{F2} = \rho \int_{V_f} x \frac{\partial \omega}{\partial t} \, dS, \quad L_{F3} = -\rho \int_{V_f} u \omega \, dS \tag{3.2c}$$

$$L_{B3} = -\rho R \oint_{\Sigma} \omega u_r \cos \theta \, d\theta. \tag{3.2d}$$

When Σ shrinks to the cylinder surface so that $V_f = 0$, (3.1) and (3.2) reduce to the boundary vorticity-flux expression (2.6), with component form

$$D = (D_{B1} + D_{B2})_{r=1}, \tag{3.3a}$$

$$L = (L_{B1} + L_{B2})_{r=1}. \tag{3.3b}$$

3.2. Numerical method and calculated forces

To obtain the solution of viscous flow over a circular cylinder, a fractional-step method was employed to solve the incompressible Navier–Stokes equations. Time

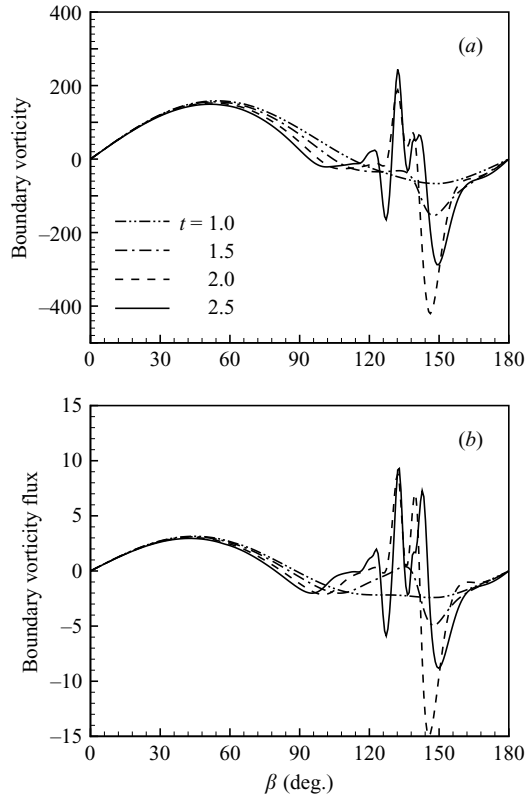


FIGURE 2. (a) Vorticity and (b) vorticity flux on the surface of the cylinder at the initial starting period. Here, $\beta \equiv \pi - \theta$ increases from the front-point of the cylinder in the clockwise direction.

advancement is performed by use of a second-order Adams–Bashforth scheme on the convective terms and a Crank–Nicolson scheme on the viscous terms. For the spatial derivatives, a third-order biased-upwind scheme (Rai & Moin 1991) and a fourth-order central scheme were used to discretize the convective and viscous terms, respectively. The discretized formulation has been described in detail, and the code validated and verified, in previous studies (e.g. Lu & Dalton 1996).

The adherence condition was imposed on the cylinder surface $r = 1$. A Neumann condition for the out-flow boundary and a Dirichlet condition for the in-flow boundary (Lu & Dalton 1996) were used at the outer boundary of the computational domain at $r = 30$, which was deemed sufficiently far from the cylinder that the influence of the computational domain size on calculated results would be negligible. This kind of outer boundary condition has been validated in the above-cited papers, and for a similar use see Mittal & Singh (2005). The Reynolds number based on the cylinder diameter was $Re = 9500$, the grid number was 512×512 with sufficiently mesh resolution inside the boundary layers to ensure that $\mu \nabla^2 \omega$ there can be calculated with enough accuracy, as required when using the diffusion form. The dimensionless time step was 0.0005. To validate the present calculation, the vorticity and vorticity flux along the cylinder are shown in figure 2 in an early stage of the flow development. It has been verified that the results agree well with those computed by Koumoutsakos & Leonard (1995).

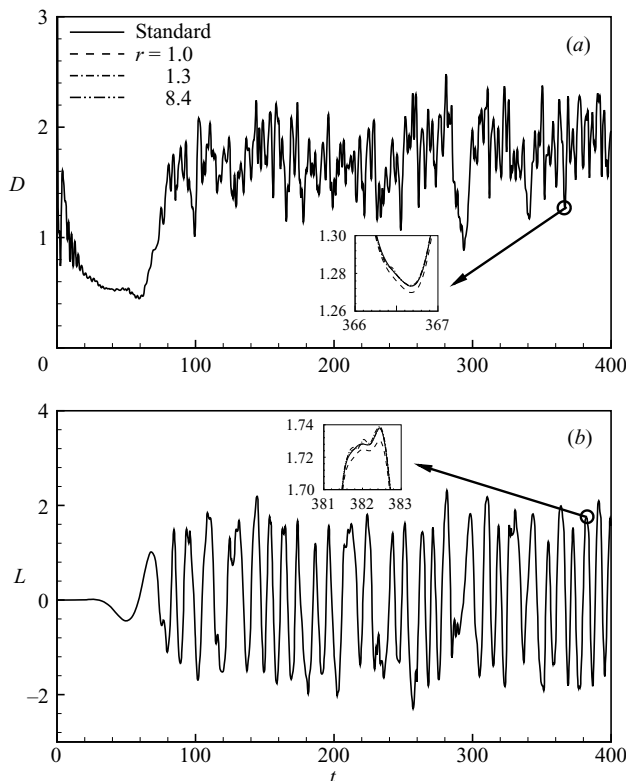


FIGURE 3. Time-dependence of (a) the drag (D) and (b) lift (L) coefficients calculated by (2.1) with different analysis domains and by the standard stress-integral formula (2.7).

The time-dependence of the lift and drag coefficients is shown in figure 3. The results were calculated by (2.1) with different analysis domains, as well as by (2.7). Both drag and lift histories collapse, yielding a single time-history curve for D and another for L . Thus, the independence of the computed forces of the analysis domain size is confirmed well. A similar comparison has been made for (2.2), with relative difference from (2.7) below 1%. In addition, it has been confirmed that D and L calculated from the finite-domain vorticity moment theory (Noca *et al.* 1999) are the same as those from (2.1) and (2.2).

4. Three-dimensional oscillatory flow over a circular cylinder

4.1. Honji instability

An oscillatory flow around a circular cylinder can be characterized by two parameters. One is the Keulegan–Carpenter number defined as $KC = U_m T/d$, and the other is the Reynolds number $Re = U_m d/\nu$, or a frequency parameter defined as $\beta = d^2/\nu T = Re/KC$, which is often used to replace the Reynolds number as an independent parameter. Here, U_m is the maximum velocity of the ambient oscillating flow, T the period of oscillation, and d the diameter of the cylinder.

In certain flow regimes, the two-dimensional oscillatory flow becomes unstable to three-dimensional disturbances (Honji 1981; Sarpkaya 1986), known as the vortical instability or Honji instability (Sarpkaya 1986). Hall (1984) assumed that

the instability was of the Taylor–Görtler type and performed a two-dimensional linear stability analysis for the limiting case of very large β and very small KC . Then, Zhang & Dalton (1999) and Lu & Ling (2003) carried out numerical simulations to examine the flow characteristics.

To non-dimensionalize the three-dimensional incompressible Navier–Stokes equations, $R = d/2$ and U_m are used as the scales of length and velocity, respectively. Then the non-dimensional equations in our computation are

$$\nabla \cdot \mathbf{u} = 0, \quad (4.1)$$

$$\frac{\partial \mathbf{u}}{\partial t} + \boldsymbol{\omega} \times \mathbf{u} = -\nabla \Phi + \frac{2}{Re} \nabla^2 \mathbf{u}, \quad (4.2)$$

where \mathbf{u} is the dimensionless velocity, t is the dimensionless time, and $\Phi = 2p/(\rho U_m^2) + |\mathbf{u}|^2/U_m^2$ is the pressure head non-dimensionalized by $\rho U_m^2/2$.

4.2. Open control surface

In the calculation we imposed a periodic condition in the axial direction (the z -direction) as usual, so that only a finite length $2L$ of the cylinder lies in the computational domain. The cylinder intersects the control surface Σ at two circles C_1 and C_2 at $z = \pm L$. Then V_f is a doubly connected domain, Σ has two circular holes, and ∂B is the cylinder surface open at two side ends. Namely, both the control surface and body surface are open surfaces. Correspondingly, (2.1) and (2.2) have to be generalized to cover this situation, in a way similar to the open-surface generalization of (2.5) (Wu & Wu 1996). After some algebra, we obtain the general diffusion and advection forms applicable to an arbitrary moving open control surface intersecting an arbitrary moving body surface:

$$\mathbf{F} = -\frac{\mu}{k} \int_{V_f} \mathbf{x} \times \nabla^2 \boldsymbol{\omega} \, dV + \mathbf{F}_B + \mathbf{F}_\Sigma + \mathbf{F}_{\text{line}}, \quad (4.3)$$

$$\mathbf{F} = -\rho \int_{V_f} \left(\frac{1}{k} \mathbf{x} \times \boldsymbol{\omega}_{,t} + \mathbf{l} \right) dV - \frac{\rho}{k} \int_{\partial V_f} \mathbf{x} \times (\mathbf{n} \times \mathbf{l}) \, dS + \mathbf{F}'_B + \mathbf{F}_\Sigma + \mathbf{F}_{\text{line}}, \quad (4.4)$$

where

$$\begin{aligned} \mathbf{F}_{\text{line}} &= \frac{1}{2} \oint_{\partial \Sigma} \mathbf{x} \times (-p \, d\mathbf{x} + 2\mu \boldsymbol{\omega} \times d\mathbf{x}) - 2\mu \oint_{\partial \Sigma} \mathbf{u} \times d\mathbf{x} \\ &= \frac{1}{2} \oint_{\partial B} \mathbf{x} \times (p \, d\mathbf{x} - 2\mu \boldsymbol{\omega} \times d\mathbf{x}) + 2\mu \oint_{\partial B} \mathbf{u} \times d\mathbf{x}, \end{aligned} \quad (4.5)$$

$$\mathbf{F}'_B = \int_{\partial B} \mathbf{x} \times \left[\mathbf{n} \times (\mathbf{b}_{,t} + \frac{1}{2} \nabla |\mathbf{b}|^2) \right] dS. \quad (4.6)$$

As a check, when Σ shrinks to coincide ∂B so that all volume integrals over V_f disappear, both (4.3) and (4.4) degenerate to the boundary vorticity-flux based force expression for an open body surface.

Now, letting the origin of the position vector be that of the cylindrical coordinates (r, θ, z) , we have $\mathbf{x} = \pm L \mathbf{e}_z + R \mathbf{e}_r$ at C_1 and C_2 , respectively. If we cut the cylinder surface along a line $\theta = \text{constant}$ so that ∂B has the same topology as a plane rectangular region, since \mathbf{n} points into the cylinder the positive $d\mathbf{x}$ -direction on C_1 is counterclockwise (right-hand rule with respect to \mathbf{e}_z), while that on C_2 is clockwise (right-hand rule with respect to $-\mathbf{e}_z$). Thus, we have $d\mathbf{x} = \pm R \mathbf{e}_\theta d\theta$ at C_1 and C_2 . Therefore, the periodic condition $f(r, \theta, L) = f(r, \theta, -L)$ for any function $f(r, \theta, z)$

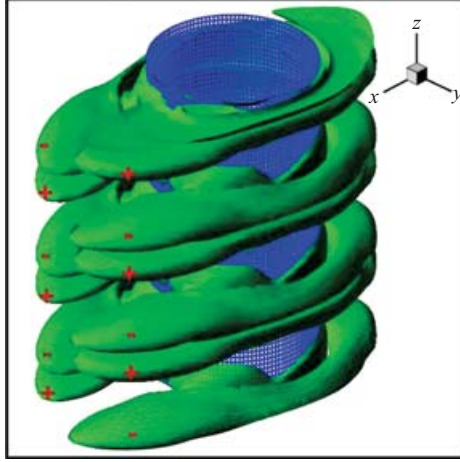


FIGURE 4. Isosurfaces of the circumferential vorticity component (ω_θ) for $\omega_\theta = 1$ (+) and -1 (−) at $t = 24T$ with T the period of oscillation.

reduces (4.5) to

$$\mathbf{F}_{\text{line}} = RL \oint_{C_1} (-p\mathbf{e}_r + 2v\omega_z\mathbf{e}_\theta) d\theta. \quad (4.7)$$

Note that owing to taking the moment, the side-boundary contribution is not completely cancelled by the periodic condition; rather, some components are doubled.

4.3. Flow structures and forces

As the frame of reference is fixed to the cylinder in the calculation, a sinusoidally oscillating flow $\mathbf{u} = \sin(\pi t/KC)\mathbf{e}_x$ was imposed at far boundary, and $\mathbf{u} = \mathbf{0}$ was set everywhere at the initial time. The adherence condition is employed on the cylinder surface, and the periodic condition is used in the circumferential and axial directions. The numerical methods for solving (4.1) and (4.2) are given by Zhang & Dalton (1999). In this study, the number of mesh points is $101 \times 129 \times 65$ in the (r, θ, z) directions with a cylinder length $L_z = 2L = 4$. The computational domain is $30R$ in the radial direction, and the time step is 0.0005. Typical results are analysed for $KC = 2$ and $\beta = 300$.

To demonstrate the three-dimensional structures due to the vortical instability, figure 4 shows the isosurfaces of the circumferential vorticity component at one instant. A well-defined axial variation of the circumferential vorticity structures with three pairs of counter-rotating vortices is shown in figure 5 by the contours of vorticity components in the (r, z) -planes at $\theta = 45^\circ, 135^\circ, 225^\circ$, and 315° . The structures are very similar to the experimental observations (Honji 1981; Sarpkaya 1986). As indicated in figures 4 and 5, the three-dimensional flow structures lie alternately on the two sides of the cylinder. In addition, we have found that the magnitude of the axial vorticity component ω_z during one cycle is about 35 or $|\omega_z|_{\text{max}} \simeq 35$, while for the other two vorticity components $|\omega_r|_{\text{max}} \simeq 2$ and $|\omega_\theta|_{\text{max}} \simeq 3$. Thus, the axial vorticity component ω_z plays a dominating role and, as shown in figure 5, its structures exhibit a quasi-two-dimensional behaviour.

Since the transverse force acting on the cylinder by the oscillating flow is a few orders smaller than the drag D , in what follows we present the drag behaviour only.

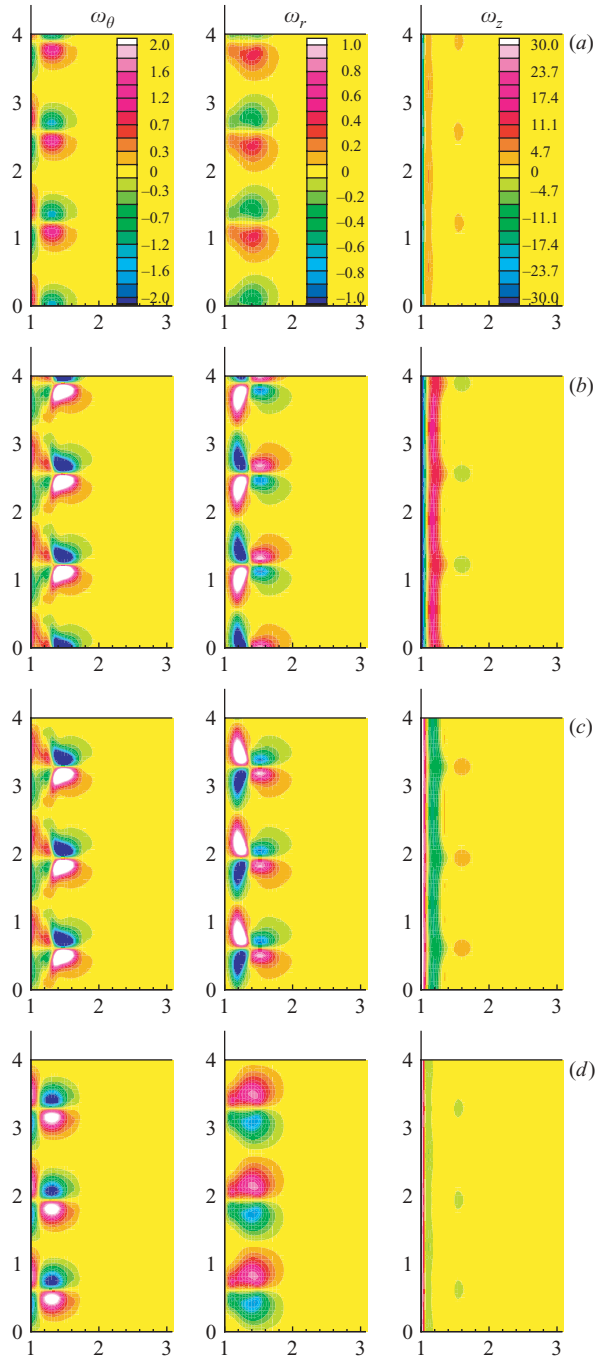


FIGURE 5. Contours of the vorticity components at $t = 24T$ in the (r, z) planes at (a) $\theta = 45^\circ$, (b) 135° , (c) 225° , and (d) 315° . Here, ω_θ , ω_r and ω_z represent the vorticity components in the circumferential, radial, and axial direction, respectively.

Figure 6 shows the time variation of D calculated for a few radii of the outer boundary of the analysis domains, which are compared with the result from (2.7). The agreement of the curves is excellent.

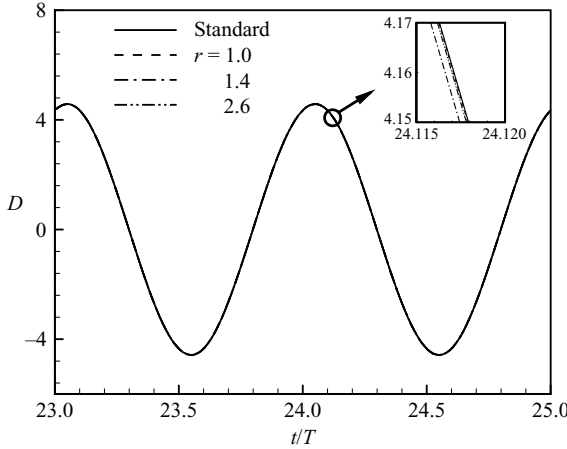


FIGURE 6. Time variation of the drag coefficient calculated by (2.1) with different analysis domains and by the standard stress-integral formula (2.7).

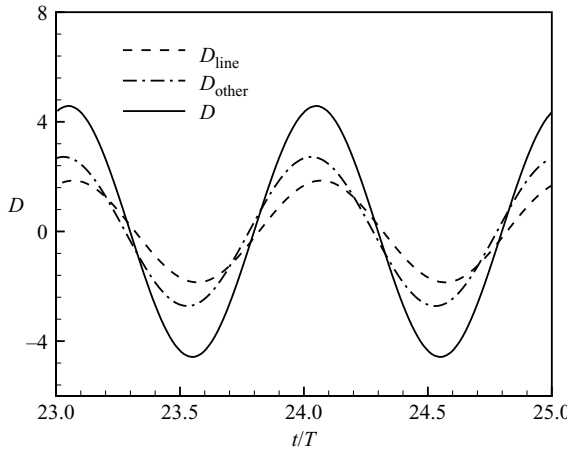


FIGURE 7. Time variation of the drag coefficient contributed by the line integral (4.7) and by the other terms of (4.3) including volume and surface integrals.

Then, in figure 7, we compare the contributions of the line integral (4.7) with the sum of the other terms of (4.3) including volume and surface integrals. The line integral is comparable with the volume and surface integrals. This situation was encountered by Wu et al. (1999) when they diagnosed the flow over a delta-wing-body combination with an open body base at the trailing edge, using the boundary vorticity-flux theory. To further display the relative magnitude of the two constituents of (4.7), figure 8 shows their respective circumferential distributions at two phases, indicating that the pressure term is dominant.

5. Effects on the force of local flow structures at their different evolution stages

Having verified the correctness and exactness of the three forms of DMT-based force expressions for both two- and three-dimensional flows, we now come to the major issue of this paper: to identify the key flow structures that have net contribution to the

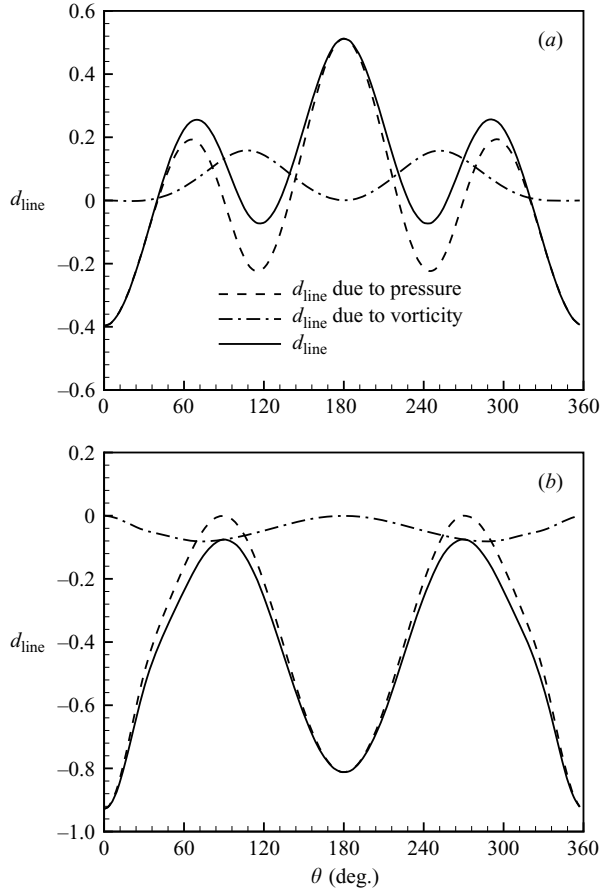


FIGURE 8. Distributions of the constituents of (4.7) related to the pressure and vorticity at two phases: (a) $t = 23.25T$ and (b) $23.5T$.

force. In circular-cylinder flows, the vortex system consists of three major structures: boundary layers, free separated shear layers before rolling up into concentrated vortices, and well-developed wake vortices. The specific structures captured by the advection and diffusion forms of the expressions are found to be different, although their integrated effects are exactly the same. While the integrand of (2.2) consists of all three of the above structures appearing in the analysis domain, the integrand of (2.1) mainly consists of the boundary layers and free separated shear layers. The behaviour of the structures inside the analysis domain evidently contains the full induced effect of those that have escaped from the domain, and the direct contribution of the latter to the total force is picked up well by the Σ -integral (2.4) and line integral (4.5). Here lies the advantage of the combined use of the three forms: to reveal the influence on the total force of local flow structures at their different evolution stages, which will be addressed in detail below.

As shown in figure 5 and remarked in §4.3, since the axial vorticity component ω_z is larger than the other two components by one order, the three-dimensional oscillating flow is still dominated by the evolution of the axial vorticity component ω_z and corresponding cross-sectional velocity components u_r and u_θ , with a phase change at different z -locations and t . The direct effect of the three-dimensionality of the vortical

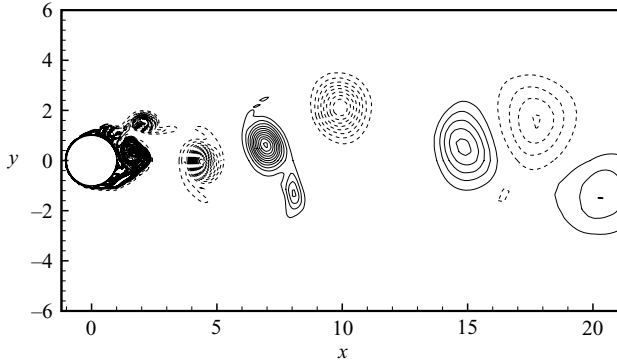


FIGURE 9. Vorticity contours from -10 to 10 with increment 0.5 . In this and the following figures, unless stated otherwise, instantaneous time is $t = 378$; solid lines represent positive values and dashed lines negative values; the vorticity varies from -278 to 194 , or simply denoted by $[-278, 194]$.

structures on the force is weak. To simplify our discussion and for clarity, therefore, we shall focus on the two-dimensional flow field obtained in § 3.

5.1. The effect of wake vortices on the force

Figure 9 shows the computed vorticity distribution in the vortex system of the two-dimensional circular-cylinder flow at an arbitrarily chosen time instant after the vortex street has become fully developed.† This kind of plot, along with the (\mathbf{u}, p) -field, is the basis of conventional flow analysis. In contrast, the field integrands of D_{F2} , D_{F3} and L_{F2} , L_{F3} in (3.2) are shown in figures 10 and 11, respectively. The boundary line integrals D_{B3} and L_{B3} (not shown here) were found to be $O(10^{-3})$ smaller. The plots in these figures capture the same vortices as those in figure 9, but their difference is worth stressing. From figure 9 alone one does not know how each moving vortex influences the force quantitatively, because on the one hand the effect of these vortices on the force is hidden in the conventional expression (2.7), but on the other hand the integrand function of DMT-based expression (2.2) or (3.2) requires much more information than merely the vorticity distribution. For example, the vorticity field has to be associated with a non-parallel local velocity field to form a non-zero Lamb-vector field; and due to the sign change of ω_x and v as a vortex passes a spatial point \mathbf{x} , the contribution of a single wake vortex may be split into two or even four pieces, with different signs.

Moreover, an inspection of the flow data indicates that the highest positive and negative peaks of D_{F2} , D_{F3} , L_{F2} , and L_{F3} (see the upper and lower bounds indicated in the captions of figures 10 and 11) are confined to the attached and free shear layers. Once the vortices are shed, their corresponding peak values are reduced by $5 \sim 10$ times. Along with the cancellation due to the aforementioned sign changes in each single vortex, we found that the wake vortices only provide about $10\% \sim 15\%$ of the total forces. Therefore, it is those layer-like structures that are the major source of the forces. This observation is consistent with the finding from the diffusion form to be discussed below.

† Unless stated otherwise, all the following figures of the cylinder flow are taken at the same time instance as in figure 9.

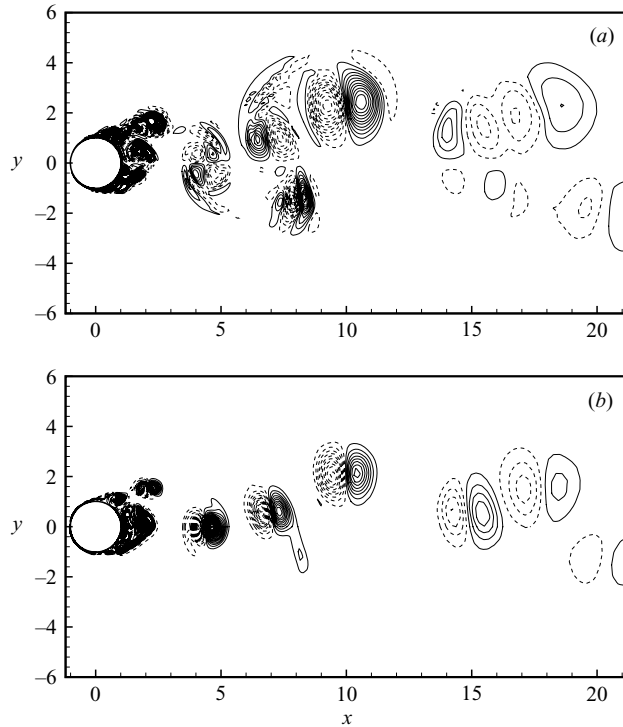


FIGURE 10. Decomposed fields of the integrand for the drag constituents: (a) integrand of $D_{F2} \in [-218, 100]$ from -20 to 20 with increment 1.0 ; (b) integrand of $D_{F3} \in [-193, 204]$ from -10 to 10 with increment 0.5 .

In passing, we mention that the integrand of L_{F2} , i.e. the unsteady term $\rho x \omega_{,t}$, does not decay as x increases. But this does not matter since in a finite domain there is no integral-convergence problem, while when Σ retreats to infinity, integral convergence has been proved in the vorticity-moment theory (Wu 1981).

5.2. The effect of boundary layers and shear layers on the force

In the diffusion form, the distribution of $\nu \nabla^2 \omega$ is under consideration. For flows at large Reynolds numbers, the peak values of $\nu |\nabla^2 \omega|$ carried by well-developed wake vortices are quite weak. The strongest peaks appear in the attached and free shear layers of thickness $\delta = O(Re^{-1/2})$ with vorticity $\omega = O(Re^{1/2})$ therein, across which $\mu |\nabla^2 \omega| \sim \mu |\omega_{,nn}| = O(Re^{1/2})$. This is shown in figure 12 for the integrand distribution of D_{F1} and L_{F1} in (4.1) for cylinder flow. The full range of values given in the caption indicates the existence of very thin and sharp positive and negative peaks of $|\nabla^2 \omega|/Re = O(10^2)$ adjacent to the wall which, if fully displayed, would smear out most other structures from the plots, see figures 12(a) and 12(b). Only when the range of values is reduced by two orders, as shown in figures 12(c) and 12(d), can abundant structures in the near wake with $|\nabla^2 \omega|/Re = O(1)$ be observed. However, these weaker structures, which are stronger than fully developed wake vortices in the vorticity diffusion sense, contribute effectively to D_{F1} and L_{F1} since they span a much larger space than those with high narrow peaks. Therefore, perhaps contrary to the conventional picture that the forces are induced by the vortex street, in terms of the diffusion form, the boundary layers and separated shear layers, just before tightly rolling up into concentrated vortices, produce about 90 % of the net contribution to

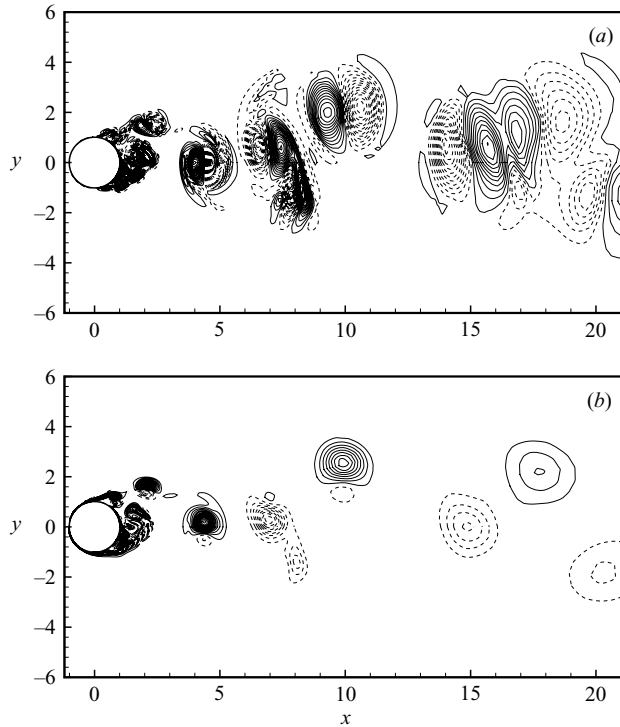


FIGURE 11. Decomposed fields of the integrand for the lift constituents: (a) integrand of $L_{F2} \in [-219, 263]$ from -80 to 80 with increment 4.0 ; (b) integrand of $L_{F3} \in [-103, 95]$ from -20 to 20 with increment 1.0 .

D and L . Once a concentrated wake vortex is formed and is shed downstream after its feeding sheet is cut off, it makes little direct contribution to the forces. Of course, the Kármán vortex street must and does strongly influence the total force; but now its major role is indirect through its induced effect on unsteadiness of the boundary-layer separation and the motion of separated shear layers.

Consequently, for flow at $Re \gg 1$, switching from the advection form to the diffusion form implies focusing on the more upstream vortical structures shown in figure 12. To capture the boundary layers and separated shear layers, the outer boundary Σ only needs to cover the wake-vortex formation region (cf. Green & Gerrard 1993), much smaller than that in figures 10 and 11.

The corresponding integrand distributions in line integrals of normal diffusion fluxes D_{B1} and L_{B1} are shown in figure 13, which contribute about 10% of D and L . Compared with these, our numerical survey shows that the integrand of D_{B2} and F_{B2} due to the azimuthal gradient of vorticity are much smaller, by an order of 10^{-3} .

It should be stressed that the possibility of capturing different local flow processes and structures by different forms lies in the fact that neither advection nor diffusion forms have a d/dt operator outside the integrals. Throughout the present paper, all derivative terms are absorbed in the integrand functions, which can therefore be expressed alternatively, as remarked in §2, by the advection or diffusion terms of the Navier–Stokes equation and vorticity transport equation.

We now return to figure 12 and notice that since, across a typical shear layer with normal variable n , $\partial^2\omega/\partial n^2$ changes sign twice, the integrand of the diffusion

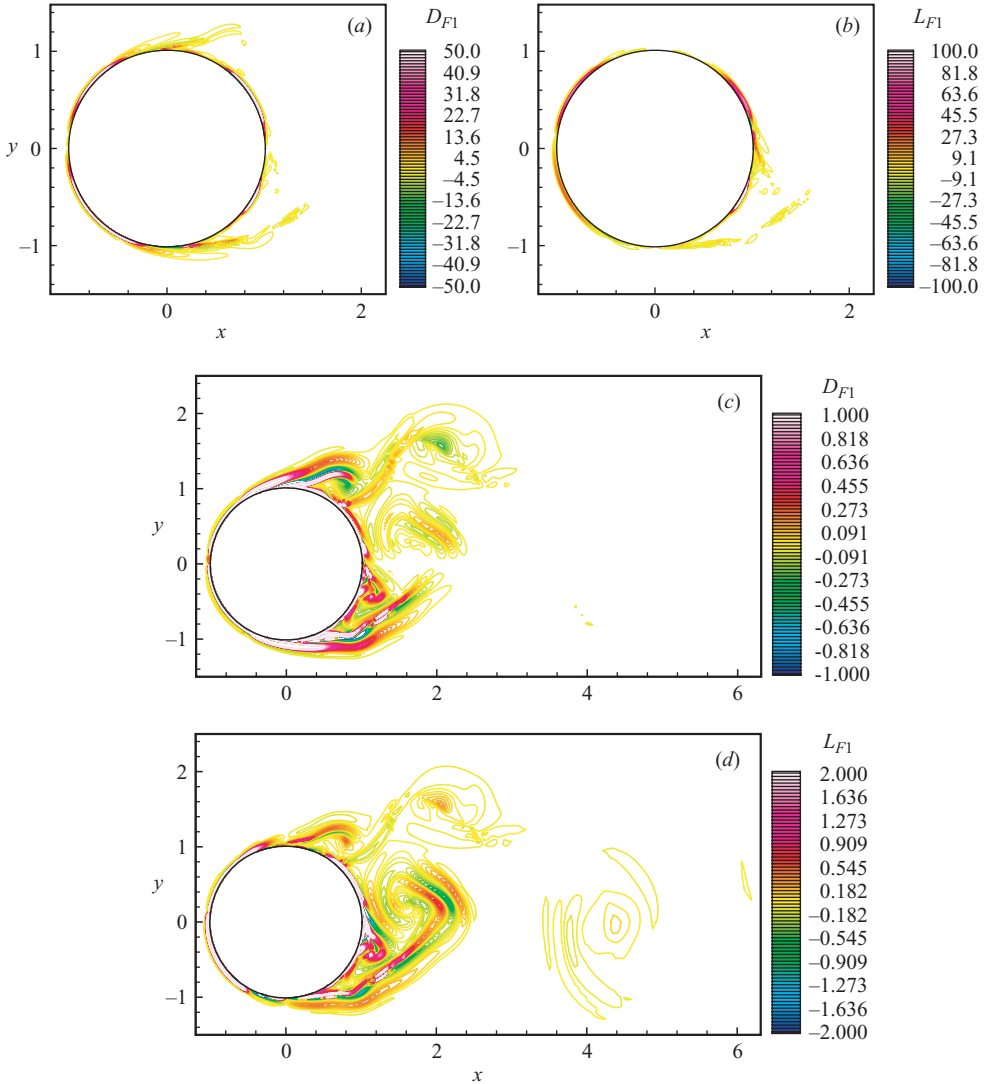


FIGURE 12. Decomposed field of the integrand for the drag and lift constituents: (a) integrand of $D_{F1} \in [-64, 183]$ from -50 to 50 ; (b) integrand of $L_{F1} \in [-343, 238]$ from -100 to 100 ; (c) integrand of $D_{F1} \in [-64, 183]$ from -1 to 1 ; (d) integrand of $L_{F1} \in [-343, 238]$ from -2 to 2 .

form appears to have a sandwich-like structure. Therefore, remarkably, in either the advection form or the diffusion form each single structure always provides both positive and negative effects on the forces. So far we have found no single structure that has purely a one-sign contribution to the forces. This situation is consistent with the well-known fact in steady attached flow that a viscous flow over an airfoil must produce boundary layers at both the upper and lower surfaces, but only the algebraic sum of the total vorticity in these layers (the net circulation) yields the desired lift. It seems that this physical fact implies the rule that there is always a ‘price to pay’, as long as the aerodynamic forces are produced by the no-slip condition, boundary layers, shear layers, and vortices. However, whether this rule is completely general for

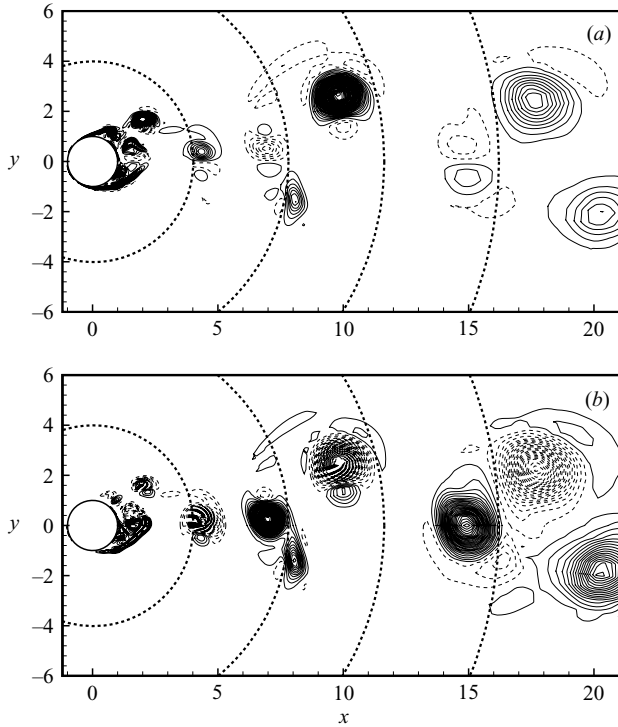


FIGURE 13. Field distributions of the integrand for the moments of viscous vorticity gradients. The boundary integrals for the drag and lift constituents can be estimated by these distributions around circles with different marked locations. (a) integrand of $D_{B1} \in [-14, 25]$ from -10 to 10 with increment 0.25 ; (b) integrand of $L_{B1} \in [-193, 105]$ from -40 to 40 with increment 1 .

any fluid-dynamic process and structure and, if so, what kind of configurations can produce flow structures with maximum favourable effect in their entire evolution, is of great interest and remains an open issue.

5.3. Correlation between boundary vorticity flux and boundary layer separation

The concept of boundary vorticity flux and its distributions on typical configurations have been extensively discussed and demonstrated in some of the cited references. The boundary vorticity flux represents an on-wall dynamic process which causes the formation of vortical structures, but itself is not a flow structure. For the present circular-cylinder flow, the variations of the integrands of the two terms of (3.3a) and (3.3b) with $\beta = \pi - \theta$, as well as their sums, are shown in figure 14. The radial component of $v\nabla\omega$ is much stronger than its azimuthal component, because they are balanced by the $O(1)$ tangent pressure gradient (recall that $v\partial\omega/\partial n = \sigma_p$ in (2.6)) and the $O(Re^{-1/2})$ skin friction, respectively. Since the integrands of D_{B1} and L_{B1} are the moments of σ_p , due to the sign change of $(x, y) = (\cos\theta, \sin\theta)$, these integrands exhibit more fluctuation than σ_p itself.

Although figure 14 directly shows that the boundary vorticity-flux peaks dominate D and L , for complex unsteady separated flows such figures alone cannot show what causes these peaks and what flow structures they cause in turn. To integrate this creation form with the above advection and diffusion forms as a whole, therefore, it is necessary to know how the boundary vorticity flux is correlated with the near-wall velocity, vorticity and vorticity derivatives.

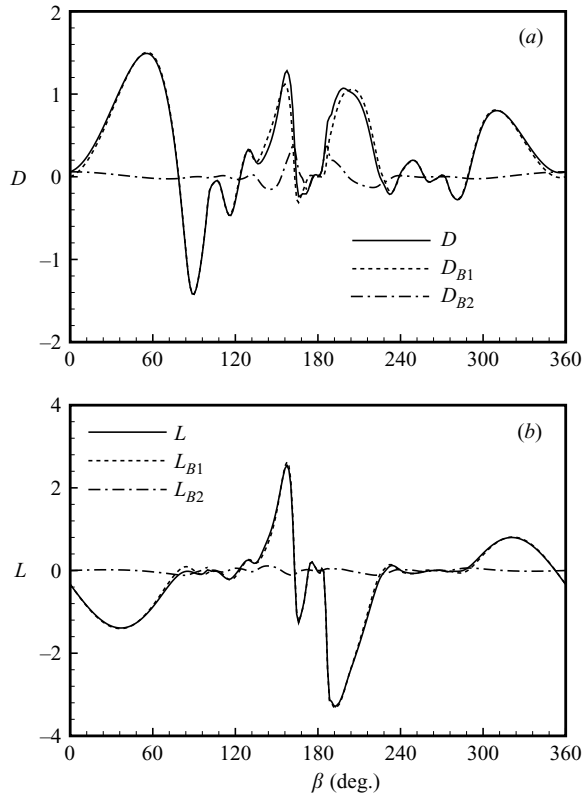


FIGURE 14. Distributions of the integrands for the moment of boundary vorticity fluxes (both normal and tangent) on the cylinder surface: (a) boundary vorticity flux for drag: solid line, D ; dashed line, D_{B1} due to normal flux; dash-dot line, D_{B2} due to tangent flux. (b) Boundary vorticity flux for lift: solid line, L ; dashed line, L_{B1} due to normal flux; dash-dot line, L_{B2} due to tangent flux.

Wu & Wu (1996) have demonstrated that generically the stress-related boundary vorticity fluxes are both the root and signature of the vortical flow. As a root, the entire vorticity field including its boundary value ω_B (and hence the skin friction) is a spatial-temporal accumulated effect of boundary vorticity flux. Thus, if there exists a boundary vorticity-flux peak at a time t_0 , a corresponding ω_B peak will appear later somewhere downstream (in the local sense). For the circular-cylinder flow, such a correlation of $\sigma = \sigma_p$ with ω_B at the early stage of the flow evolution can be recognized by comparing the curves in figures 2(a) and 2(b). As a signature of the flow, however, the stress-related boundary vorticity fluxes are in turn determined by the entire flow field, so more information than that presented in figure 2 is necessary for a full understanding of the correlation.

Inspecting a temporal correlation requires considering the time evolution of the fields around t_0 . Thus, to exhibit clearly the double role of the boundary vorticity flux as both the root and signature of the flow, we display the upper half of the cylinder flow at a sequence of three time instants in figure 15. At each instant the figure shows the local patterns of σ , ω_B , the velocity profiles, as well as the contours of $\omega(x)$ and $\nabla^2\omega(x)/Re$. The driving mechanism of σ is the near-wall advection. Once again, the full range of values $\nabla^2\omega/Re$ with large positive and negative peaks should be noticed.

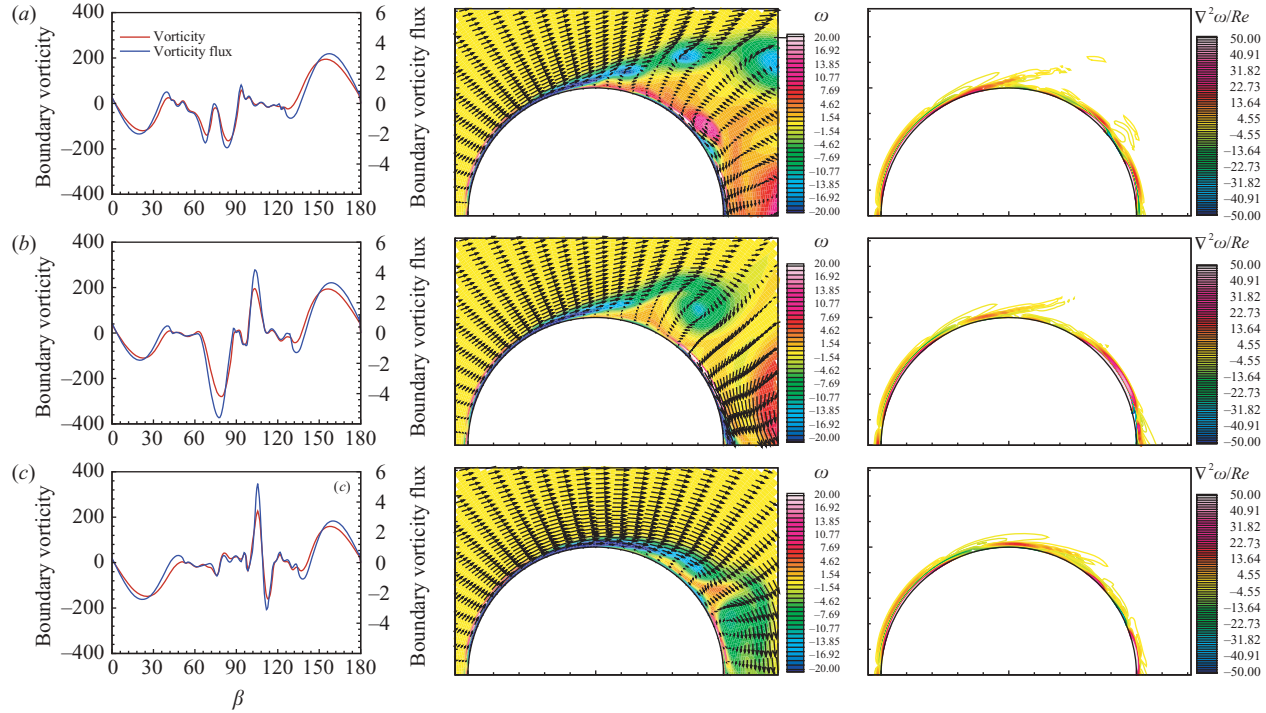


FIGURE 15. Boundary vorticity and boundary vorticity-flux profiles, vorticity contours and velocity vectors, and contours of the vorticity diffusion term: (a) $t = 376$, $\omega \in [-162, 193]$, $\nabla^2 \omega / Re \in [-95, 123]$; (b) $t = 378$, $\omega \in [-278, 194]$, $\nabla^2 \omega / Re \in [-217, 244]$; (c) $t = 380$, $\omega \in [-158, 225]$, $\nabla^2 \omega / Re \in [-253, 267]$.

Similarly, weak structures with $|\nabla^2\omega|/Re = O(1)$ are consistent with figures 12(c) and 12(d).

As shown in figure 15(a) at $t = 376$, $\sigma < 0$ upstream of the primary separation at $\beta = \pi - \theta \sim 80^\circ$, owing to the favourable on-wall pressure gradient. The former generates negative ω_B with a small spatial-temporal phase lag. Then, a secondary strong negative σ peak occurs around $\beta \sim 75^\circ$ due to the downwash mainly caused by the strong, nearest counterclockwise wake vortex shed from the lower surface (a portion of this vortex is seen at the lower right corner of the vorticity contour).

The primary separated shear layer rolls up into a clockwise vortex. At $t = 378$, the vortex becomes stronger under the same downwash and induces a secondary separation with an associated adverse pressure gradient or positive σ peak at $\beta \sim 105^\circ$ (figure 15b). This also grows strongly and causes an upwelling that almost cuts off the sheet feeding the primary vortex at $t = 380$ (figure 15c). A positive ω_B peak follows the σ peak again with a small spatial-temporal phase lag in the local flow direction. This spatial-temporal correlation of σ and ω_B continues at larger θ ; but between $\beta \sim 130^\circ$ and 180° the phase lag is reversed, as is the local flow direction, shown by the velocity profiles in figure 15(c).

The corresponding picture represented by the plots of $\nabla^2\omega$ follows from the vorticity contours. The aforementioned characteristics of this vorticity diffusion term, i.e. that it is strong only before rolling up into concentrated vortices, and appears as having a sandwich structure, are further demonstrated.

From the above discussion, the three kinds of expressions, i.e. the advection form, the diffusion form, and the creation form, are connected to form a complete physical picture. Different structures and on-wall quantities in these forms belong to the same vortex system, and their behaviours are dynamically consistent.

6. Concluding remarks

The conventional integrated force and moment expressions are the starting point rather than the final form of an aerodynamic theory. The requirement to understand extremely complex flow structures and to perform highly accurate flow analysis requires a bridge between integral performance and local dynamics, including local processes and structures. An effective and widely applicable way to do this is applying derivative-moment transformations to the conventional integral expressions. The resulting unconventional expressions have a rich variety of forms, permitting one to choose a specific form for a special purpose. For the theoretical development, Wu's (1981) vorticity moment theory provides a natural platform; if the flow is steady, the advection form is convenient (WMZ). For experimental measurements, the finite-domain extension of Wu's theory and especially the unsteady force expression for control-surface integral alone, due to Noca *et al.* (1999), are most convenient. For flow diagnosis based on numerical simulation, it is advantageous to keep all the derivative terms inside the integrals to pinpoint the local processes and flow structures responsible for the forces. This approach yields three force expressions as explored in this paper.

The three expressions have been tested for two unsteady separated flows over a circular cylinder. Based on our numerical solutions, all three forms give the same integrated results with high accuracy for both flows. The results are also independent of the size of the external boundary of the analysis domain.

How the local flow processes and structures influence the forces has been investigated. The three forms capture different vortical structures and on-wall quantities

at different evolution stages of the whole vortex system produced by the cylinder, ranging from the wake vortices to the boundary vorticity flux on the body surface. Each of these forms has advantages and shortcomings. The boundary vorticity-flux expression is a direct alternative to the conventional surface-stress expression, easy to calculate and use in configuration diagnosis and design, but lacks information on the of flow structures which produce the vorticity flux. On the other hand, the advection form can reveal the respective contributions of all structures of the vortex system within the analysis domain, including the wake vortices which only have a minor net contribution to the forces, and is also easy to compute as it involves only the first spatial derivative of the velocity field. The diffusion form is intermediate, which enables focusing on the layer-like structures in a smaller domain before the wake vortices are well-formed; but the Laplacian of vorticity requires computing the third-order derivatives as an expense. The choice of form depends on the need and available data; but whenever possible a joint use of these forms will provide a rich multi-view dynamic picture of the role of the evolving vortical wake in determining the forces.

The present study has also extended the rule that there is always a price to pay, observed for steady attached flow to unsteady separated flow: as long as the forces are produced through the no-slip condition, boundary layers, shear layers and vortices, it is impossible for any single structure to have a solely favourable effect on the desired force without any negative influence. Therefore, various engineering configurations that work by producing vortical flows or involving such flows may not be ultimately the best with the highest possible efficiency; seeking the optimal flow mechanisms with minimum side effects among all possible means in fluid dynamics still remains a significant open issue.

This work was supported in part by the Innovation Project of the Chinese Academy of Sciences (No. KJCX-SW-L04), the National Natural Science Foundation of China (Nos. 10332040, 10572005, 10532010, 90405007), and Program for Changjiang Scholars and Innovative Research Team in Universities. The authors are very grateful to Professors James C. Wu, Chui-Jie Wu, and Roy Schulz for the valuable discussions, as well as very helpful comments made by the referees on an early version of the paper.

REFERENCES

- BACHELOR, G. K. 1967 *An Introduction to Fluid Dynamics*. Cambridge University Press.
- BIRCH, J. M. & DICKINSON, M. H. 2003 The influence of wing-wake interactions on the production of aerodynamic forces in flapping flight. *J. Expl Biol.* **206**, 2257–2272.
- GRAZIANI, G. & BASSANINI, P. 2002 Unsteady viscous flows about bodies: Vorticity release and forces. *Meccanica* **37**, 283–303.
- GREEN, R. B. & GERRARD, J. H. 1993 Vorticity measurements in the near wake of a circular cylinder at low Reynolds numbers. *J. Fluid Mech.* **246**, 675–691.
- GUO, M., LI, Q., HOU, A., & YUAN, W. 2006 A diagnosis and design approach of axial compressor based on local dynamics. *ASME Turbo Expo. 2006: Power for Land, Sea and Air, May 8–11, 2006, Barcelona, Spain*. GT2006-91116.
- HALL, P. 1984 On the stability of the unsteady boundary layer on a cylinder oscillating transversely in a viscous fluid. *J. Fluid Mech.* **146**, 347–367.
- HONJI, H. 1981 Streaked flow around an oscillating circular cylinder. *J. Fluid Mech.* **107**, 509–520.
- JEON, D. & GHARIB, M. 2001 On circular cylinders undergoing two-degree-freedom forced motions. *J. Fluids Struct.* **15**, 533–541.

- KOUMOUTSAKOS, P. & LEONARD, A. 1995 High-resolution simulations of the flow around an impulsively started cylinder using vortex method. *J. Fluid Mech.*, **296**: 1–38.
- LAMB, H. 1932 *Hydrodynamics*. Dover.
- LI, Q. S. & GUO, M. 2005 The diagnosis and design of a low-speed compressor based on local dynamics. *Prog. Natural Sci.* **15**, 221–228.
- LIGHTHILL, M. J. 1986 *An Informal Introduction to Theoretical Fluid Dynamics*. Oxford University Press.
- LU, X. Y. & DALTON, C. 1996 Calculation of the timing of vortex formation from an oscillating cylinder. *J. Fluids Struct.* **10**, 527–541.
- LU, X. Y. & LING, G. C. 2003 Three-dimensional instability of an oscillating viscous flow past a circular cylinder. *Appl. Math. Mech.* **24**, 791–800.
- MITTAL, S. & SINGH, S. 2005 Vortex-induced vibrations at subcritical *Re*. *J. Fluid Mech.* **534**, 185–194.
- NOCA, F., SHIELDS, D. & JEON, D. 1999 A comparison of methods for evaluating time-dependent fluid dynamic forces on bodies, using only velocity fields and their derivatives. *J. Fluids Struct.* **13**, 551–578.
- PLOUMHANS, P., WINCKELMANS, G. S., SALMON, J. K., LEONARD, A. & WARREN, M. S. 2002 Vortex methods for direct numerical simulation of three-dimensional bluff body flows: Application to the sphere at $Re = 300, 500$, and 1000. *J. Comput. Phys.* **178**, 427–463.
- RAI, M. M. & MOIN, P. 1991 Direct simulations of turbulent flow using finite-difference schemes. *J. Comput. Phys.* **96**, 15–53.
- SAFFMAN, P. G. 1992 *Vortex Dynamics*. Cambridge University Press.
- SARPKAYA, T. 1986 Force on a circular cylinder in viscous oscillatory flow at low Keulegan-Carpenter numbers. *J. Fluid Mech.* **165**, 61–71.
- TAN, B. T., THOMPSON, M. C. & HOURIGAN, K. 2005 Evaluating fluid forces on bluff bodies using partial velocity data. *J. Fluids Struct.* **20**, 5–24.
- THOMSON, J. J. 1883 *A Treatise on the Motion of Vortex Rings*. Macmillan, London.
- TRUESDELL, C. 1954 *The Kinematics of Vorticity*. Indiana University Press.
- WU, J. C. 1981 Theory for aerodynamic force and moment in viscous flows. *AIAA J.* **19**, 432–441.
- WU, J. C. 2005 *Elements of Vorticity Aerodynamics*. Tsinghua University Press, Beijing.
- WU, J. Z., MA, H. Y. & ZHOU, M. D. 2006 *Vorticity and Vortex Dynamics*. Springer (referred to herein as WMZ).
- WU, J. Z., PAN, Z. L. & LU, X. Y. 2005 Unsteady fluid-dynamic force solely in terms of control-surface integral. *Phys. Fluids* **17**, 098102.
- WU, J. Z., ROACH, R. L., LO, C. F., ZHU, F. L., DOWGWILLO, R. M., JIANG, L. B. & TRAMEL, R. W. 1999 Aerodynamic diagnostics and design based on boundary vorticity dynamics. *AIAA Paper* 99-3103.
- WU, J. Z. & WU, J. M. 1993 Interactions between a solid surface and a viscous compressible flow field. *J. Fluid Mech.* **254**, 183–211.
- WU, J. Z. & WU, J. M. 1996 Vorticity dynamics on boundaries. *Adv. Appl. Mech.* **32**, 119–275.
- ZHANG, J. F. & DALTON, C. 1999 The onset of three-dimensionality in an oscillating flow past a fixed circular cylinder. *Intl. J. Numer. Meth. Fluids* **30**, 19–42.
- ZHU, F. L. 2000 Applications of boundary vorticity dynamics to flow simulation, airfoil design, and flow control. PhD Dissertation, University of Tennessee, Knoxville.
- ZHU, G., BEARMAN, P. W. & GRAHAM, J. M. R. 2002 Prediction of drag and lift using velocity and vorticity fields. *Aero. J.* **106**, 547–554.